Chemical Engineering Journal 157 (2010) 451–465

Contents lists available at ScienceDirect

Chemical Engineering Journal

journal homepage: www.elsevier.com/locate/cej

# CFD modelling of phenol biodegradation by immobilized *Candida tropicalis* in a gas–liquid–solid three-phase bubble column

Xiaoqiang Jia[a,b], Xue Wang[a], Jianping Wen[a,b,*], Wei Feng[a], Yan Jiang[a]

[a] *Department of Biochemical Engineering, School of Chemical Engineering and Technology, Tianjin University, Tianjin 300072, PR China*
[b] *Key Laboratory of Systems Bioengineering (Tianjin University), Ministry of Education, Tianjin 300072, PR China*

ARTICLE INFO

*Article history:*
Received 11 June 2009
Received in revised form 5 December 2009
Accepted 7 December 2009

*Keywords:*
Multiphase reaction
Phenol biodegradation
Mathematical modelling
Bubble column
Dynamic simulation
CFD

ABSTRACT

A three-dimensional transient model, combining three-phase fluid flow, interphase mass transfer and intrinsic bioreaction kinetics, was developed to simulate the dynamic behaviors of batch phenol biodegradation by immobilized *Candida tropicalis* in a gas–liquid–solid three-phase bubble column (BC). A computational fluid dynamics (CFD) method was used, with a multiple size group model adopted to determine the bubble size distribution, based on a previous three-phase BC hydrodynamic CFD model [1]. Current simulation results of phenol and oxygen concentration changes in the liquid phase were validated by corresponding experimental measurements under various operating conditions. Furthermore, local transient batch phenol biodegradation characteristics such as the oxygen concentration profiles in the gas, liquid and solid phases, the phenol concentration profiles in the liquid and solid phases, and the cell concentration profile in the solid phase were predicted. Comparisons between species interphase mass transfer and bioreaction rates were carried out to identify the rate-limiting step in the immobilized batch phenol biodegradation processes.

## 1. Introduction

Phenol is a common pollutant of industrial wastewaters from oil refineries, petrochemical plants, coking plants, brown coal distilling plants, wood manufacturing plants and phenolic-resin industries. Accumulation of phenol in an ecosystem can cause harmful effects so it is necessary to treat this waste before its safe discharge to water [2].

Biological treatment is a feasible method for removal of phenol from wastewater because of its low cost and avoidance of secondary pollution, especially at relatively low concentrations, compared with physicochemical methods [3]. Reactions with immobilized microbial cells are attracting more attention, as they may offer several advantages over processes with suspended biomass, including protecting cells from toxic substances and preventing suspended particles from joining the effluent stream [4]. Moreover, immobilized cells can be reused and can be easily separated from the reaction mixture [5]. Various types of solid matrices, such as polyacrylamide gels, alginate gels, porous glass, etc., have been used for immobilization of whole cells to maintain a high concentration of microorganisms in reactors [6–13]. Immobilization of cells with polyvalent salts of alginate has received the most attention because of the low cost and the mild conditions involved [14–17].

Bubble columns (BCs) have found wide applications over the years as cost-effective reactors for many industrial bioreactions [18]. Recently, numerous experimental investigations have indicated that BCs have very good performance in phenol biodegradation processes, both in gas–liquid (G–L) two-phase systems and in gas–liquid–solid (G–L–S) three-phase systems [19–26]. However, the understanding of this complex system, combining multiphase fluid flow, interphase mass transfer and intrinsic bioreaction, is rather limited, which prevents better optimization and scale-up of the process [27].

Computational fluid dynamics (CFD) has been adopted in the last decade as a useful tool to aid understanding of the multiphase hydrodynamics of BCs and, to a large extent, it can replace time-consuming and expensive experiments [28–33]. The current focus is on the modelling of multiphase bioreaction processes, for example, phenol biodegradation. However, most reports to date have been limited to the modelling of fluid hydrodynamics in G–L BCs [34–44] and only Feng et al. [45] in our lab have successfully developed a three-dimensional (3D) transient CFD model for simulating the local dynamic behaviors of phenol biodegradation in G–L BC using free cells. Until now, reports published on modelling of the fluid hydrodynamics of G–L–S BCs, let alone the G–L–S phenol biodegradation processes, have been very limited [46–48].

---

* Corresponding author at: Department of Biochemical Engineering, School of Chemical Engineering and Technology, Tianjin University, 92 Weijin Road, Naikai District, Tianjin 300072, PR China. Tel.: +86 22 27890492; fax: +86 22 27403389.

*E-mail addresses:* xqjia@tju.edu.cn (X. Jia), wunianshijian@hotmail.com (X. Wang), jpwen@tju.edu.cn (J. Wen), phonewell@tom.com (W. Feng), yanjiang88@126.com (Y. Jiang).

1385-8947/$ – see front matter © 2009 Elsevier B.V. All rights reserved.
doi:10.1016/j.cej.2009.12.007

**Nomenclature**

| | |
|---|---|
| $A$ | growth associated constant for phenol consumption |
| $a$ | specific area ($m^{-1}$) |
| $B$ | non-growth associated constant for phenol consumption ($s^{-1}$) |
| $C$ | concentration ($kg\,m^{-3}$) |
| $D$ | kinematic diffusivity ($m^2\,s^{-1}$) |
| $d$ | diameter (m) |
| $g$ | gravitational acceleration ($m\,s^{-2}$) |
| $K$ | mass transfer coefficient ($m\,s^{-1}$) |
| $K_i$ | phenol inhibition constant ($kg\,m^{-3}$) |
| $K_o$ | oxygen half-saturation constant ($kg\,m^{-3}$) |
| $K_s$ | phenol half-saturation constant ($kg\,m^{-3}$) |
| $S$ | source term ($kg\,m^{-3}\,s^{-1}$) |
| $Sc_T$ | turbulence Schmidt number |
| $t$ | time (s) |
| $\mathbf{u}$ | velocity vector ($m\,s^{-1}$) |
| $x$ | mass fraction |
| $Y_{x/o}$ | cell growth yield based on oxygen |

*Greek letters*

| | |
|---|---|
| $\alpha$ | volume fraction |
| $\varepsilon$ | turbulence eddy dissipation ($m^2\,s^{-3}$) |
| $\Gamma$ | mass transfer source term ($kg\,m^{-3}\,s^{-1}$) |
| $\mu$ | molecular viscosity (Pa s) |
| $\mu_{\max}$ | maximum specific cell growth rate ($s^{-1}$) |
| $\mu_T$ | turbulence induced viscosity (Pa s) |
| $\rho$ | density ($kg\,m^{-3}$) |

*Superscripts*

| | |
|---|---|
| * | saturated state |
| – | dimensionless state |

*Subscripts*

| | |
|---|---|
| 0 | initial state |
| $a$ | alginate gel |
| $g$ | gas phase |
| $l$ | liquid phase |
| $m$ | mineral salt medium |
| $n$ | nitrogen |
| $o$ | oxygen |
| $p$ | phenol |
| $s$ | solid phase |
| sup | superficial |
| $x$ | cell |

Until recently, bubbles were usually considered to be uniformly distributed in the multiphase reactor but with progress in model development, the evolution of bubble size distribution (BSD) and bubble–bubble interactions can now be taken into account, both of which play very significant roles in calculation of the G–L specific interfacial area [49–54]. With the so-called multiple size group (MUSIG) model, bubble sizes result directly from the population balance equation and bubble–bubble interactions are controlled by bubble coalescence and breakup laws [55,56].

The objective of this study was to develop a 3D transient CFD model for simulating the dynamic behaviors of batch phenol biodegradation with immobilized *Candida tropicalis* in alginate gel beads in a G–L–S three-phase BC. This required coupling of three-phase fluid flow, interphase species mass transfer and intrinsic bioreaction kinetics, with the BSD determined by applying the MUSIG model. Model simulation results of phenol and oxygen concentration changes in the liquid phase were validated by corresponding experimental measurements under various operating conditions. Local transient phenol biodegradation behaviors, such as hydrodynamic characteristics and species distributions, were predicted by the model and the rate-limiting step was determined through comparisons between interphase mass transfer and bioreaction of species.

## 2. Model development

In the immobilized batch phenol biodegradation process, solid carriers are suspended in the liquid phase. Oxygen is transferred from the gas phase into the liquid phase and both phenol and oxygen are transferred from the liquid phase into the solid phase, where they are consumed by cells. The solid particles are assumed to be spherical, with a single, constant radius during the biodegradation process, while cells are distributed uniformly within the alginate gel beads. Substrate degradation and cell growth within the alginate gel beads are both limited by phenol and oxygen concentrations, while all other nutrients are in excess. The influence of free cells in the liquid phase on phenol biodegradation is negligible because they are present only in very small amounts [57].

Based on the above considerations, a 3D transient CFD model was developed to simulate the batch phenol biodegradation dynamic behaviors by immobilized *C. tropicalis* in a G–L–S three-phase BC, combining three-phase fluid flow, interphase species mass transfer and intrinsic bioreaction kinetics. An Eulerian approach was adopted to describe the flow behavior of each phase. The liquid phase, composed of mineral salt medium, phenol and oxygen, was considered to be the continuous phase, while the gas phase, composed of nitrogen and oxygen, and the solid phase, composed of alginate gel, phenol, oxygen and cells, were considered to be the dispersed phases. A turbulence model, simulating the local transient hydrodynamics as well as the MUSIG model describing the BSD, were previously presented in detail [1] so is not repeated here.

### 2.1. Species transport equations

The following provides a detailed description of the species transport equations and the corresponding model parameters:

$$\frac{\partial}{\partial t}(\rho_g\alpha_g x_{o,g}) + \nabla\cdot(\rho_g\alpha_g x_{o,g}\boldsymbol{u}_g) = \nabla\cdot\left[\alpha_g\left(\rho_g D_{o,g} + \frac{\mu_{T,g}}{Sc_{T,g}}\right)(\nabla x_{o,g})\right] - \Gamma_{o,gl} \tag{1}$$

$$\frac{\partial}{\partial t}(\rho_l\alpha_l x_{o,l}) + \nabla\cdot(\rho_l\alpha_l x_{o,l}\boldsymbol{u}_l) = \nabla\cdot\left[\alpha_l\left(\rho_l D_{o,l} + \frac{\mu_{T,l}}{Sc_{T,l}}\right)(\nabla x_{o,l})\right] + \Gamma_{o,gl} - \Gamma_{o,ls} \tag{2}$$

$$\frac{\partial}{\partial t}(\rho_l\alpha_l x_{p,l}) + \nabla\cdot(\rho_l\alpha_l x_{p,l}\boldsymbol{u}_l) = \nabla\cdot\left[\alpha_l\left(\rho_l D_{p,l} + \frac{\mu_{T,l}}{Sc_{T,l}}\right)(\nabla x_{p,l})\right] - \Gamma_{p,ls} \tag{3}$$

$$\frac{\partial}{\partial t}(\rho_s\alpha_s x_{o,s}) + \nabla\cdot(\rho_s\alpha_s x_{o,s}\boldsymbol{u}_s) = \nabla\cdot\left[\alpha_s\left(\rho_s D_{o,s} + \frac{\mu_{T,s}}{Sc_{T,s}}\right)(\nabla x_{o,s})\right] - S_{o,s} + \Gamma_{o,ls} \tag{4}$$

$$\frac{\partial}{\partial t}(\rho_s\alpha_s x_{p,s}) + \nabla\cdot(\rho_s\alpha_s x_{p,s}\boldsymbol{u}_s) = \nabla\cdot\left[\alpha_s\left(\rho_s D_{p,s}+\frac{\mu_{T,s}}{Sc_{T,s}}\right)(\nabla x_{p,s})\right] - S_{p,s} + \Gamma_{p,ls} \tag{5}$$

$$\frac{\partial}{\partial t}(\rho_s\alpha_s x_{x,s}) + \nabla\cdot(\rho_s\alpha_s x_{x,s}\boldsymbol{u}_s) = \nabla\cdot\left[\alpha_s\left(\rho_s D_{x,s}+\frac{\mu_{T,s}}{Sc_{T,s}}\right)(\nabla x_{x,s})\right] + S_{x,s} \tag{6}$$

where $\rho$ is the density of each phase, $\alpha$ is the volume fraction of each phase, $x$ is the mass fraction of each species in a given phase, $\mathbf{u}$ is the velocity vector of each phase, $D$ is the kinematic diffusivity of each species in a given phase, $\mu_T$ is the turbulence viscosity of each phase, $Sc_T$ is the turbulence Schmidt number of each phase, with the default value of 0.9 [58], $S$ is the reaction source term of each species, and $\Gamma$ is the interphase mass transfer source term of each species. The subscripts $g$, $l$, and $s$ denote the gas, liquid and solid phase, respectively; $o$, $p$ and $x$ denote oxygen, phenol and cell species, respectively.

Nitrogen was considered to be the constraint component in the gas phase; the mineral salt medium was considered to be the constraint component in the liquid phase; and alginate gel was considered to be the constraint component in the solid phase. The species balance in each phase is given by the following equations:

$$x_{o,g} + x_{n,g} = 1 \tag{7}$$

$$x_{o,l} + x_{p,l} + x_{m,l} = 1 \tag{8}$$

$$x_{o,g} + x_{p,s} + x_{x,s} + x_{a,s} = 1 \tag{9}$$

where the subscripts $n$, $m$ and $a$ denote the nitrogen, mineral salt medium and alginate gel species, respectively.

The gas phase oxygen kinematic diffusivity, $D_{o,g} = 2\times10^{-5}\,\mathrm{m^2\,s^{-1}}$, the liquid phase oxygen kinematic diffusivity, $D_{o,l} = 2.54\times10^{-9}\,\mathrm{m^2\,s^{-1}}$ and the liquid phase phenol kinematic diffusivity, $D_{p,l} = 8.69\times10^{-9}\,\mathrm{m^2\,s^{-1}}$ [59]. The solid phase oxygen and phenol kinematic diffusivities were calculated using the random-pore model in the presence of cells [57]:

$$D_{o,s} = D_{o,l}[1 - 2.6\times10^{-3}(\rho_s x_{x,s})^{-}]^2 \tag{10}$$

$$D_{p,s} = D_{p,l}[1 - 2.6\times10^{-3}(\rho_s x_{x,s})^{-}]^2 \tag{11}$$

Note that the cell concentration in the solid phase, $(\rho_s x_{x,s})^{-}$, is in the dimensionless state in the above two equations. The solid phase cell kinematic diffusivity, $D_{x,s}$, was regarded to be 0.

Haldane's equation proved to be suitable for simulating the intrinsic cell growth kinetics of free cells of *C. tropicalis* when phenol is the sole carbon source and exhibits inhibition effects under high concentration [60]. As this study was carried out for an immobilized cell system, the oxygen limitation effect had to be taken into account for better simulation pf the cell growth behavior within the alginate gel beads, which is expressed by the Monod equation [61]. The reaction source term of each species in the solid phase can then be written as:

$$S_{x,s} = \alpha_s\mu_x(\rho_s x_{x,s}) = \alpha_s\frac{\mu_{\max}(\rho_s x_{p,s})}{K_s + (\rho_s x_{x,s}) + (\rho_s x_{x,s})^2/K_i}\cdot \times\frac{\rho_s x_{o,s}}{K_o + (\rho_s x_{o,s})}(\rho_s x_{x,s}) \tag{12}$$

$$S_{p,s} = \alpha_s[A\mu_x(\rho_s x_{x,s}) + B(\rho_s x_{x,s})] = A\cdot S_{x,s} + \alpha_s B\cdot(\rho_s x_{x,s}) \tag{13}$$

$$S_{o,s} = \frac{S_{x,s}}{Y_{x/o}} \tag{14}$$

where $\mu_{\max}$ is the maximum specific cell growth rate, $K_s$ is the phenol half-saturation constant, $K_i$ is the phenol inhibition constant, $K_o$ is the oxygen half-saturation constant, $A$ is the growth associated constant for phenol consumption, $B$ is the non-growth associated constant for phenol consumption and $Y_{x/o}$ is the cell growth yield based on oxygen. These intrinsic bioreaction kinetic parameters were obtained from previous studies and the literature, with $\mu_{\max} = 1.33\times10^{-4}\,\mathrm{s^{-1}}$, $K_s = 1.17\times10^{-2}\,\mathrm{kg\,m^{-3}}$, $K_i = 2.08\times10^{-1}\,\mathrm{kg\,m^{-3}}$, $A = 8.23\times10^{-1}$, $B = 7.69\times10^{-5}\,\mathrm{s^{-1}}$ [60], $K_o = 2.6\times10^{-4}\,\mathrm{kg\,m^{-3}}$ and $Y_{x/o} = 4.65\times10^{-1}$ [61]. The species interphase mass transfer source term is:

$$\Gamma_{o,gl} = K_{o,gl}a_g[(\rho_l x^*_{o,l}) - (\rho_l x_{o,l})] \tag{15}$$

$$\Gamma_{o,ls} = K_{o,ls}a_s[(\rho_s x^*_{o,s}) - (\rho_s x_{o,s})] \tag{16}$$

$$\Gamma_{p,ls} = K_{p,ls}a_s[(\rho_s x^*_{p,s}) - (\rho_s x_{p,s})] \tag{17}$$

The gas–liquid oxygen mass transfer coefficient, $K_{o,gl}$, was calculated by [62]:

$$K_{o,gl} = \frac{2}{\sqrt{\pi}}\sqrt{D_{o,l}}\left(\frac{\varepsilon\rho_l}{\mu_l}\right)^{0.25} \tag{18}$$

where $\varepsilon$ is the liquid phase turbulence eddy dissipation and $\mu$ is the molecular viscosity.

The liquid–solid oxygen mass transfer coefficient, $K_{o,ls}$, and the liquid–solid phenol mass transfer coefficient, $K_{o,ps}$, were calculated by the following correlations [63]:

$$K_{o,ls} = \frac{D_{o,l}}{d_s}\left\{2 + 0.695\left(\frac{\mu_l}{\rho_l D_{o,l}}\right)^{1/3}\left[\frac{u_{g,\mathrm{sup}}g d_s^4}{(\mu_l/\rho_l)^3}\right]^{0.2}\right\} \tag{19}$$

$$K_{p,ls} = \frac{D_{p,l}}{d_s}\left\{2 + 0.695\left(\frac{\mu_l}{\rho_l D_{p,l}}\right)^{1/3}\left[\frac{u_{g,\mathrm{sup}}g d_s^4}{(\mu_l/\rho_l)^3}\right]^{0.2}\right\} \tag{20}$$

The liquid phase saturated oxygen mass fraction at the specified gas phase oxygen mass fraction, $x^*_{o,l}$, the solid phase saturated oxygen mass fraction at the specified liquid phase oxygen mass fraction, $x^*_{o,s}$, and the solid phase saturated phenol mass fraction at the specified liquid phase oxygen mass fraction, $x^*_{p,s}$, were calculated through the mass fraction equilibrium ratio of oxygen and phenol between the gas–liquid interphase and the liquid–solid interphase, respectively.

The gas bubble specific area was calculated by $a_g = 6\alpha_g/d_g$ and the solid bead specific area was calculated by $a_s = 6\alpha_s/d_s$.

The phase density, $\rho$, molecular viscosity, $\mu$, volume fraction, $\alpha$, velocity vector, $\mathbf{u}$, turbulence viscosity, $\mu_T$, and the liquid phase turbulence eddy dissipation, $\varepsilon$ and the Sauter mean bubble diameter, $d_g$, were all obtained from the turbulence model, combined with the MUSIG model presented previously [1].

The species transport due to interphase mass transfer and bioreaction is small compared with the main body of each phase, thus its effects on the continuity equations and the momentum equations were neglected [58].

### 2.2. Initial and boundary conditions

Transient calculations start from the assumptions that each phase velocity is 0 m/s, the gas volume fraction is 0 and the solid particles distribute uniformly within the reactor. Initial phenol concentrations in the liquid phase $C_{p,0} = 0.1$, 0.15 and 0.2 kg m$^{-3}$, initial phenol concentration in the solid phase was 0 kg m$^{-3}$; initial cell concentration in the solid phase was 9 kg m$^{-3}$; initial oxygen volume fraction in the gas phase was 0.21; initial oxygen concentrations in the liquid phase and the solid phase were

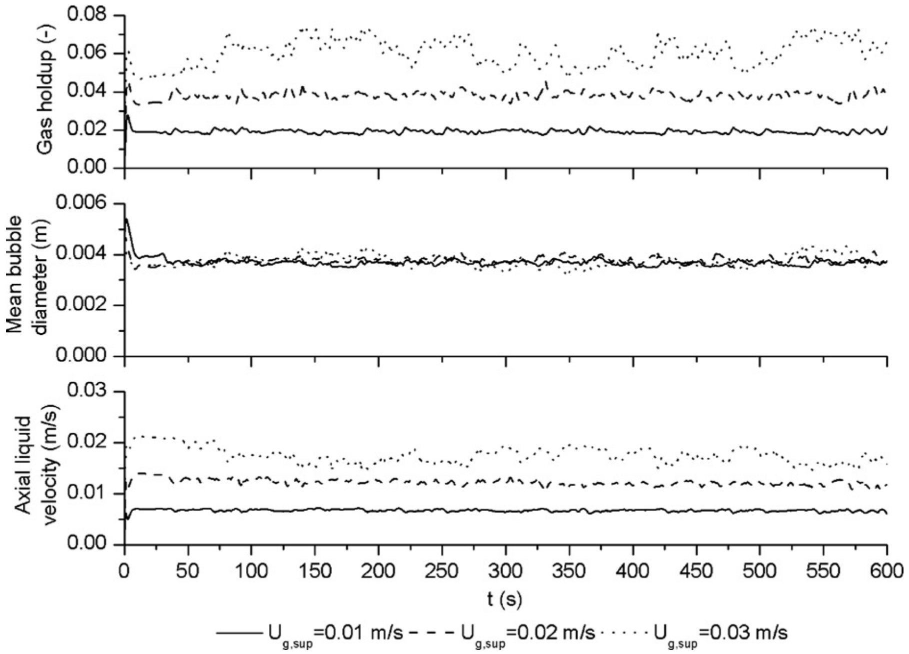

**Fig. 1.** Time courses of volume-averaged $\alpha_g$, $d_g$ and $u_w$ under different $U_{g,\text{sup}} = 0.01, 0.02, 0.03$ m/s and fixed $C_{p,0} = 150$ mg/L, $\alpha_{s,0} = 0.02$.

$7.56 \times 10^{-3}$ kg m$^{-3}$ (saturated oxygen concentration at 30 °C and normal pressure), solid loading $\alpha_{s,0} = 1$, 2 and 3% (volume fraction).

The superficial gas velocity $U_{g,\text{sup}} = 0.01$, 0.02, and 0.03 m/s, then the inlet gas velocities were determined according to the area of the distributor plate, with a gas holdup of unity and a size fraction of the 3rd bubble group (diameter 4.5 mm) set to be unity for the inlet condition [1]. The boundary condition for the walls was defined as no-slip for the continuous phase and free-slip for the dispersed phases. The modelling has to be done in a defined computation domain, but the volume of the liquid change with the change in the superficial gas velocity. To conciliate these two aspects, a proper outlet condition at the top of the column was defined, which was firstly proposed by Padial et al. [64] and was also successfully adopted by Michele and Hempel [48]: the periphery area is defined as the opening boundary where only liquid can leave the computation domain; the inner area is defined as the degassing boundary where only gas can leave the computation domain; the solid is kept within the reactor [1,58].

### 2.3. Numerical solution

In order to numerically solve the partial and ordinary differential equations, a "high-resolution" discretisation of the equations was carried out using a finite volume scheme with a coupled multi-grid

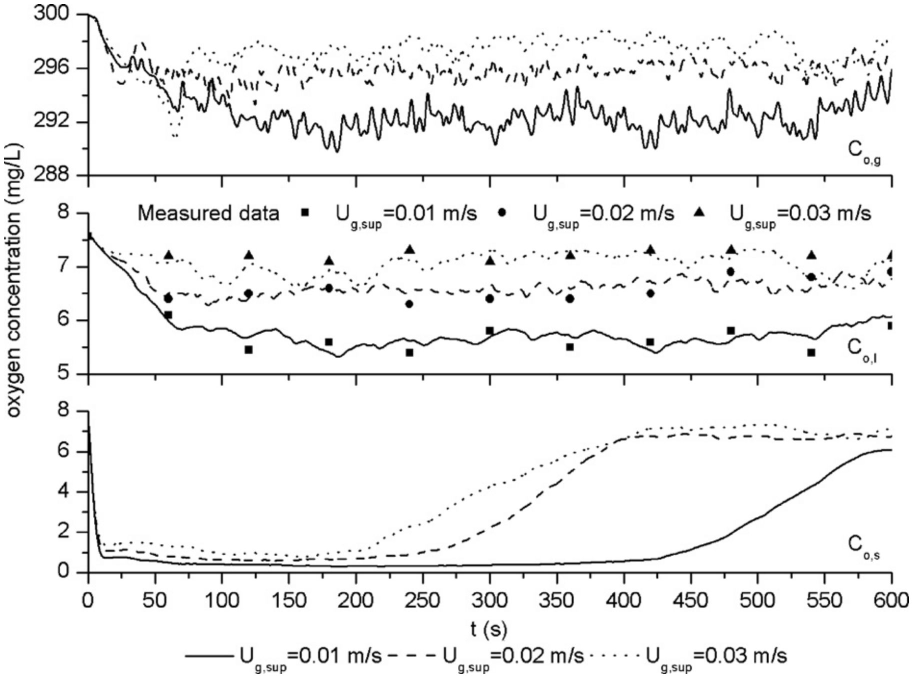

**Fig. 2.** Time courses of volume-averaged $C_{o,g}$, $C_{o,l}$ and $C_{o,s}$ under different $U_{g,\text{sup}} = 0.01, 0.02, 0.03$ m/s and fixed $C_{p,0} = 150$ mg/L, $\alpha_{s,0} = 0.02$.

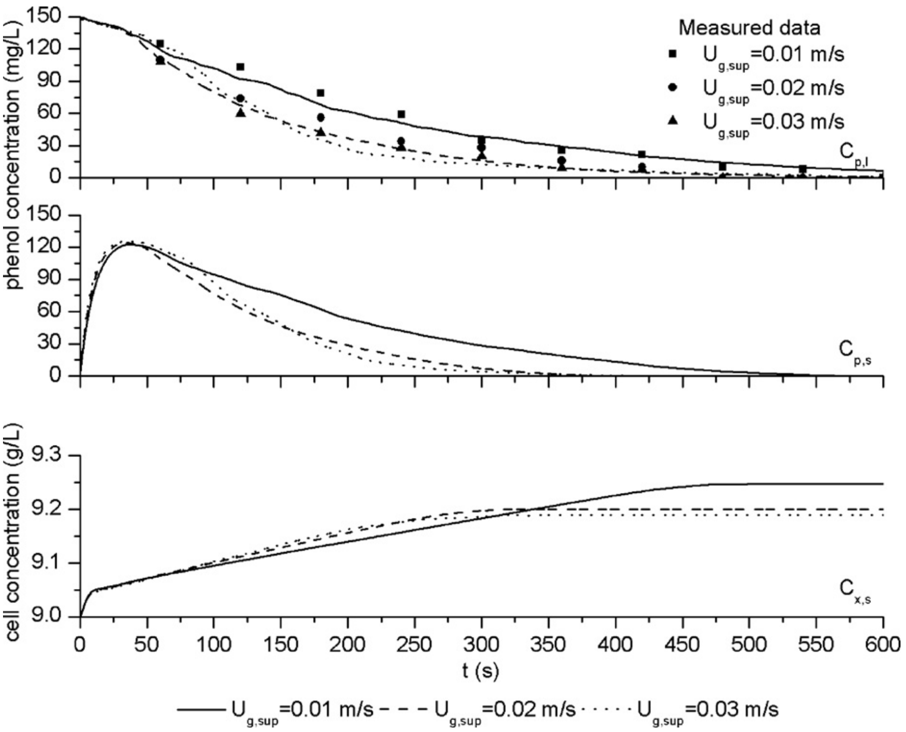

**Fig. 3.** Time courses of volume-averaged $C_{p,l}$, $C_{p,s}$ and $C_{x,s}$ under different $U_{g,\text{sup}}$ = 0.01, 0.02, 0.03 m/s and fixed $C_{p,0}$ = 150 mg/L, $\alpha_{s,0}$ = 0.02.

solver, as implemented in the commercial CFD code CFX. Unstructured grids of 10 mm × 10 mm × 15 mm, 5 mm × 10 mm × 15 mm and 5 mm × 5 mm × 15 mm were implemented with a total number of 17,640 cells within the 0.2 m × 0.2 m × 0.6 m computation domain [1]. To save computing cost, a time-stepping strategy was adopted [65], with 100 steps at 0.001 s, 100 steps at 0.002 s, 100 steps at 0.005 s, 100 steps at 0.01 s, 100 steps at 0.02 s and 100 steps at 0.05 s. For the remaining time the time step length was 0.1 s. A typical solver run over 600 s of computer time took about 400 h on an Intel Pentium D 3.0 GHz processor. Convergence was good at the criteria of $1 \times 10^{-4}$ for all variables calculated.

## 3. Methods and materials

### 3.1. Microorganism and culture conditions

A pure culture of the yeast *C. tropicalis* stored in our lab was used in this study. The yeast was isolated with the ability to utilize phenol as a sole carbon source and could tolerate very high phenol concentrations, up to 2 kg m$^{-3}$. Liquid cultures were grown in a mineral salt medium containing 0.5 kg m$^{-3}$ phenol at 30 °C in a rotary shaker at 200 rpm. The liquid mineral salt medium contained (kg m$^{-3}$): 0.4 $K_2HPO_4$, 0.2 $KH_2PO_4$, 0.1 NaCl, 0.1 $MgSO_4$,

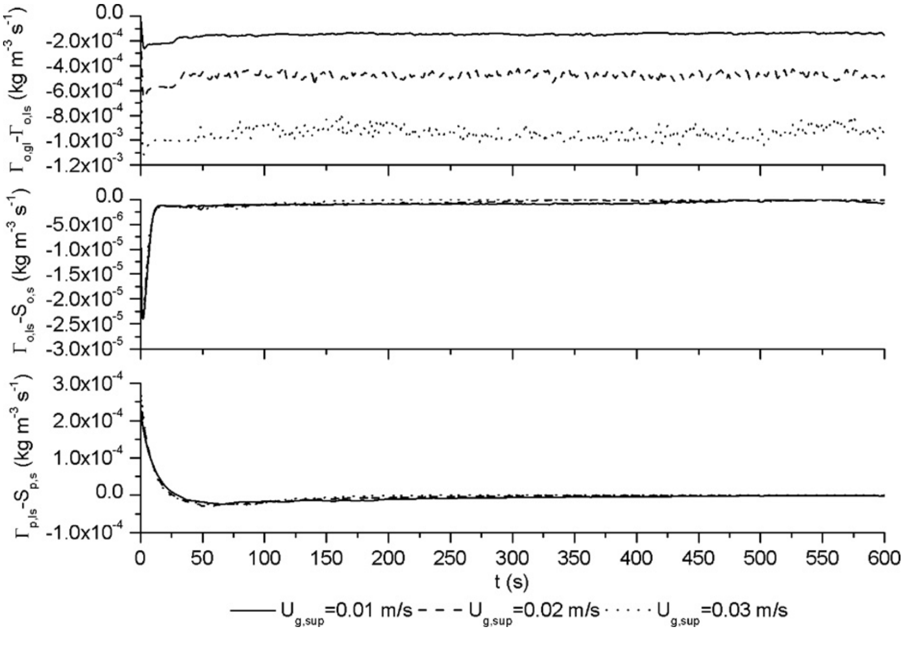

**Fig. 4.** Time courses of volume-averaged $\Gamma_{o,gl} - \Gamma_{o,ls}$, $\Gamma_{o,ls} - S_{o,s}$ and $\Gamma_{p,ls} - S_{p,s}$ under different $U_{g,\text{sup}}$ = 0.01, 0.02, 0.03 m/s and fixed $C_{p,0}$ = 150 mg/L, $\alpha_{s,0}$ = 0.02.

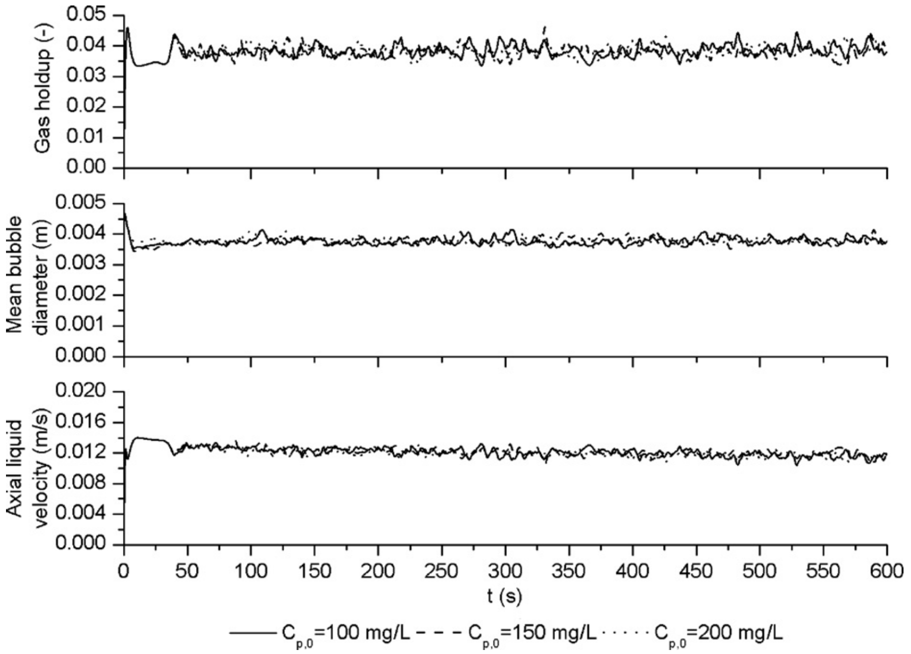

**Fig. 5.** Time courses of volume-averaged $\alpha_g$, $d_g$ and $u_w$ under different $C_{p,0} = 100, 150, 200$ mg/L and fixed $U_{g,\text{sup}} = 0.02$ m/s, $\alpha_{s,0} = 0.02$.

0.01 $MnSO_4{\cdot}H_2O$, 0.01 $Fe_2(SO_4)_3{\cdot}H_2O$, 0.01 $Na_2MoO_4{\cdot}2H_2O$ and 0.4 $(NH_4)_2SO_4$ (pH = 6.0). Phenol was sterilized by filtering through membranes (pore size $2 \times 10^{-7}$ m) and added to the medium before inoculation [60]. The cell concentration in the liquid mineral salt medium was monitored spectrophotometrically, while cell concentration on a dry weight basis was measured by filtering the cell suspension with a filter and drying the filter paper and cells to a constant weight for 24 h at 105 °C. A linear relationship between the dry cell weight and the optical density (OD) was obtained as: cell concentration (kg m$^{-3}$) = 0.35 × OD-6.92 × $10^{-4}$ [66].

### 3.2. Immobilization procedure

Sodium alginate at 2% (w/v) was used for the immobilization of the *C. tropicalis* cells. An inoculum of cell suspension at the late exponential phase (OD = 1.3, cell concentration = 0.45 kg m$^{-3}$) was centrifuged and then added into the sterilized sodium alginate at room temperature to make a cell concentration of 9 kg m$^{-3}$. Then the alginate/cell mixture was agitated uniformly and extruded aseptically through a needle into a stirred solution of sterile 0.1 M calcium chloride. The height of the needle and rate of stirring of the calcium chloride solution were adjusted carefully so that uni-

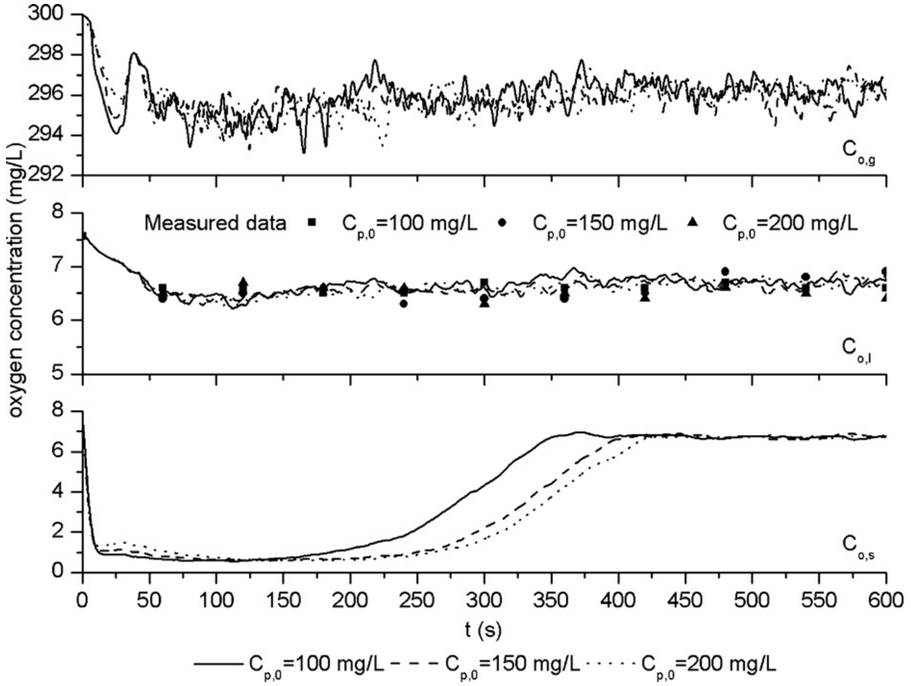

**Fig. 6.** Time courses of volume-averaged $C_{o,g}$, $C_{o,l}$ and $C_{o,s}$ under different $C_{p,0} = 100, 150, 200$ mg/L and fixed $U_{g,\text{sup}} = 0.02$ m/s, $\alpha_{s,0} = 0.02$.

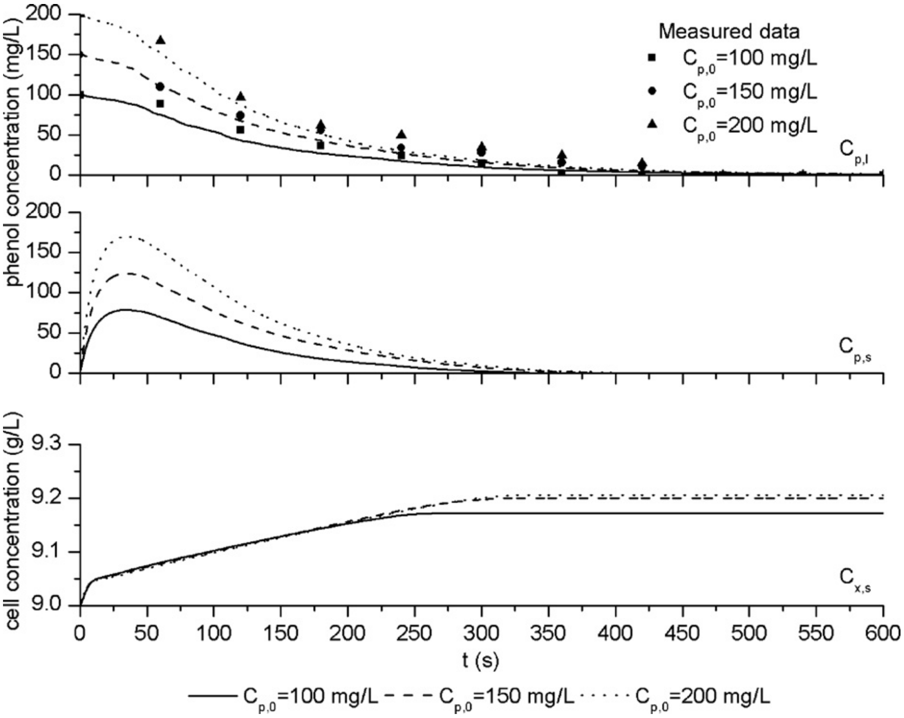

**Fig. 7.** Time courses of volume-averaged $C_{p,l}$, $C_{p,s}$ and $C_{x,s}$ under different $C_{p,0}$ = 100, 150, 200 mg/L and fixed $U_{g,\mathrm{sup}}$ = 0.02 m/s, $\alpha_{s,0}$ = 0.02.

form spherical alginate gel beads were obtained with an average diameter of $3.5 \times 10^{-3}$ m. Beads were left to harden in the calcium chloride solution for 2 h for complete replacement of sodium ions by calcium ions. The apparent density was evaluated by putting a number of alginate gel beads in a 50 mL glass cylinder, giving a value of 1048 kg m$^{-3}$.

### 3.3. Batch phenol biodegradation in a three-phase BC

The experimental apparatus was the same as that used by Feng et al. in our lab [45]. The column had a square cross-section of 0.2 m × 0.2 m and a height of 1 m. A square stainless steel perforated distributor plate with a width of 0.05 m, containing 625 holes (diameter $5 \times 10^{-4}$ m), was centrally located at the bottom of the column. Liquid mineral salt medium was the liquid phase, with a static height of 0.6 m. Liquid phase physical properties were taken to be the same as those of pure water, according to the correlations proposed by Escobedo and Mansoori [67]. Air (79% nitrogen and 21% oxygen by volume) was the gas phase with superficial gas velocities of 0.01, 0.02 and 0.03 m/s. The air was filtered with an air filter column and then introduced into the column via the gas diffuser, flow rate measured by a rotor flow meter. At the out-

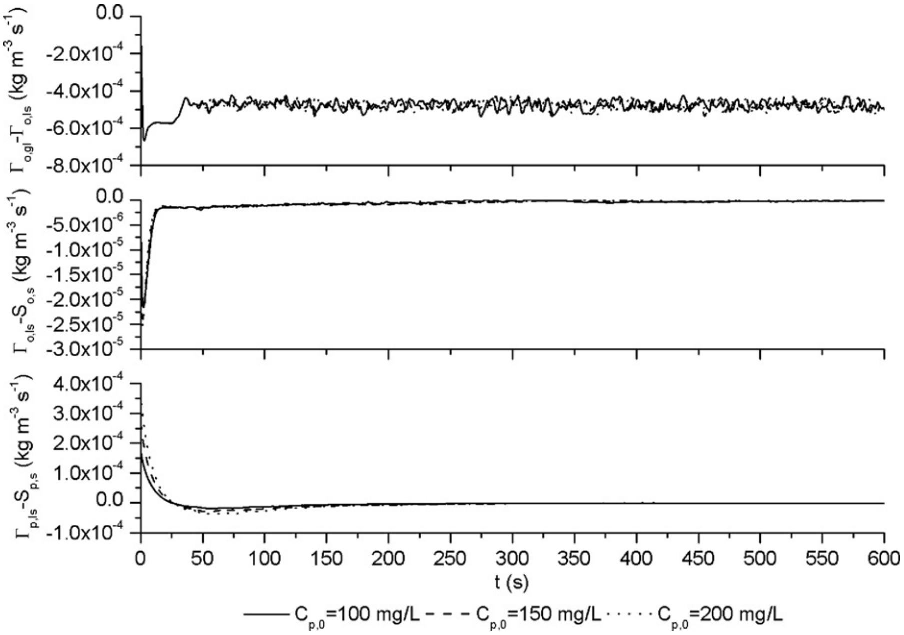

**Fig. 8.** Time courses of volume-averaged $\Gamma_{o,gl} - \Gamma_{o,ls}$, $\Gamma_{o,ls} - S_{o,s}$ and $\Gamma_{p,ls} - S_{p,s}$ under different $C_{p,0}$ = 100, 150, 200 mg/L and fixed $U_{g,\mathrm{sup}}$ = 0.02 m/s, $\alpha_{s,0}$ = 0.02.

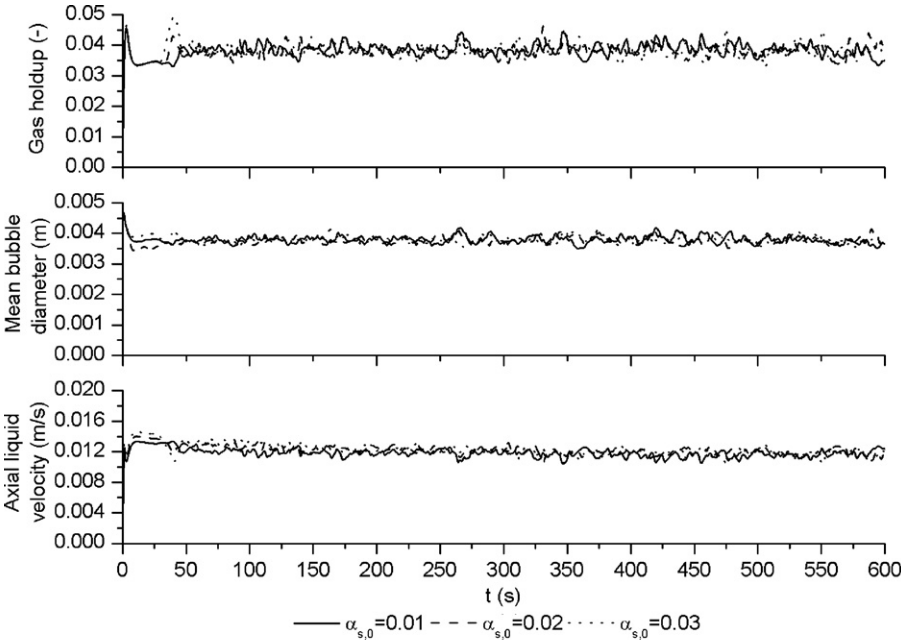

**Fig. 9.** Time courses of volume-averaged $\alpha_g$, $d_g$ and $u_w$ under different $\alpha_{s,0}$ = 0.01, 0.02, 0.03 and fixed $U_{g,\mathrm{sup}}$ = 0.02, $C_{p,0}$ = 150 mg/L.

let of the column, a filter was also used to protect the BC from being contaminated. Alginate gel beads containing cells were the solid phase, with bead loadings of 1, 2 and 3%. After washing with deionized water and sterilized mineral salt medium, batch phenol biodegradation by immobilized *C. tropicalis* was performed in the three-phase BC for initial phenol concentrations of 0.1, 0.15, and 0.2 kg $m^{-3}$. The initial pH was 6.0 and the temperature was maintained at 30 °C by circulating heated water through a water jacket. Samples were taken at several locations along the column periodically for the measurement of phenol and oxygen concentrations in the liquid phase. The measurement of phenol concentration was achieved using an HPLC method presented previously [60]. The measurement of oxygen concentration was performed by an absolute oxygen electrode (Mettler Toledo 6050, Switzerland). Each measurement was repeated three times and the data shown in the corresponding figures were the average ones.

## 4. Results and discussion

### 4.1. Model simulation of time courses of the volume-averaged process variables

The developed CFD model was used initially to simulate the time courses of the volume-averaged dynamic behaviors of the

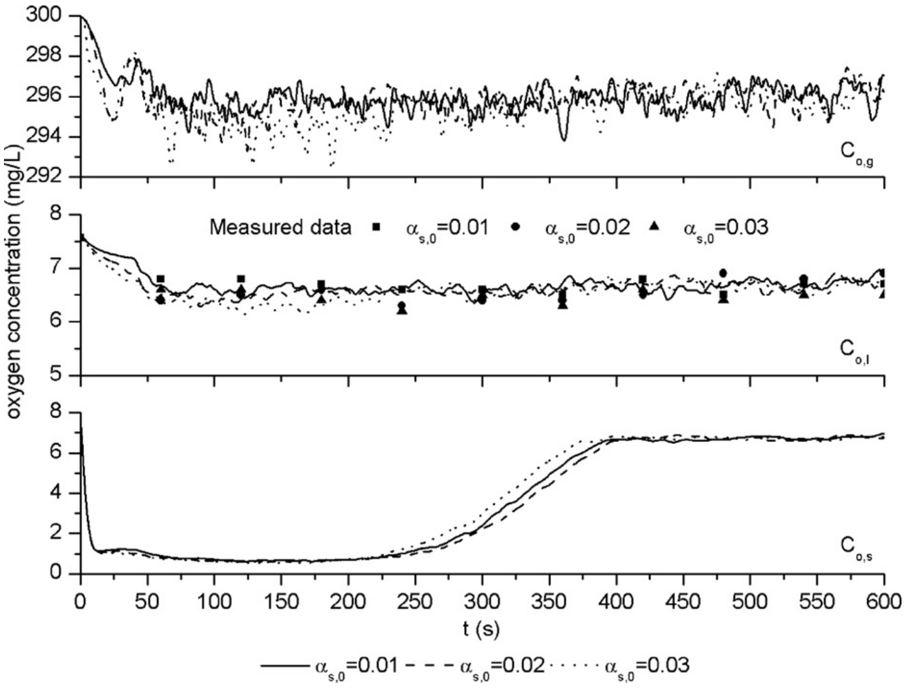

**Fig. 10.** Time courses of volume-averaged $C_{o,g}$, $C_{o,l}$ and $C_{o,s}$ under different $\alpha_{s,0}$ = 0.01, 0.02, 0.03 and fixed $U_{g,\mathrm{sup}}$ = 0.02, $C_{p,0}$ = 150 mg/L.

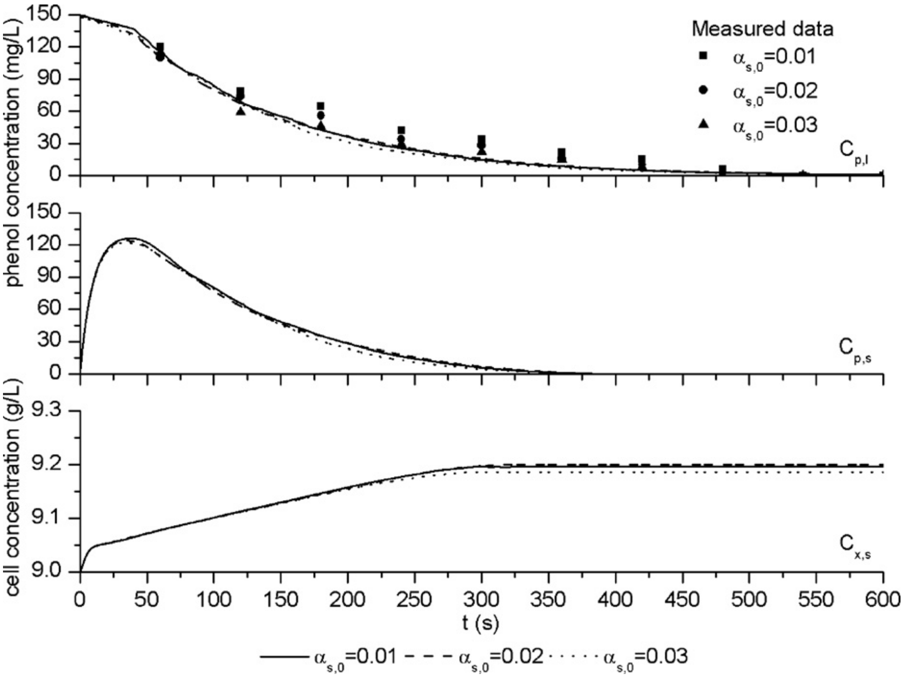

**Fig. 11.** Time courses of volume-averaged $C_{p,l}$, $C_{p,s}$ and $C_{x,s}$ under different $\alpha_{s,0}$ = 0.01, 0.02, 0.03 and fixed $U_{g,\mathrm{sup}}$ = 0.02, $C_{p,0}$ = 150 mg/L.

immobilized batch phenol biodegradation in the three-phase BC, including hydrodynamic characteristics and species mass concentrations, as shown in Figs. 1–12 under different operating conditions. Oxygen and phenol concentrations in the liquid phase were measured experimentally and used to compare with the model simulation results for validation in Figs. 2, 3, 6, 7, 10 and 11. The overall validation of the model simulation results for the liquid phase oxygen and phenol concentrations was satisfactory. For liquid phase phenol concentration comparisons, the correlation coefficient, $R^2$, is larger than 0.986 in all cases. For liquid phase oxygen concentration comparisons, the correlation coefficient, $R^2$, is larger than 0.801 in most cases, except for values of 0.629, obtained at $C_{p,0}$ = 150 mg/L, $\alpha_{s,0}$ = 0.02 and $U_{g,\mathrm{sup}}$ = 0.03 m/s, as shown in Fig. 2 and 0.774, obtained at $C_{p,0}$ = 150 mg/L, $\alpha_{s,0}$ = 0.03 and $U_{g,\mathrm{sup}}$ = 0.02 m/s, as shown in Fig. 10. The relatively low correlation coefficients for oxygen concentration comparisons compared with phenol concentration comparisons may be attributed to the low sensitivity of the DO electrode measurement compared with the HPLC method.

Figs. 1–4 show the time courses of the volume-averaged hydrodynamic characteristics, such as gas holdup $\alpha_g$, mean bubble diameter $d_g$ and axial liquid velocity $u_w$. These figures also show the volume-averaged species mass concentrations, such as gas phase oxygen concentration $C_{o,g}$, liquid phase oxygen concentration $C_{o,l}$, liquid phase phenol concentration $C_{p,l}$, solid phase oxygen concentration $C_{o,s}$, solid phase phenol concentration $C_{p,s}$

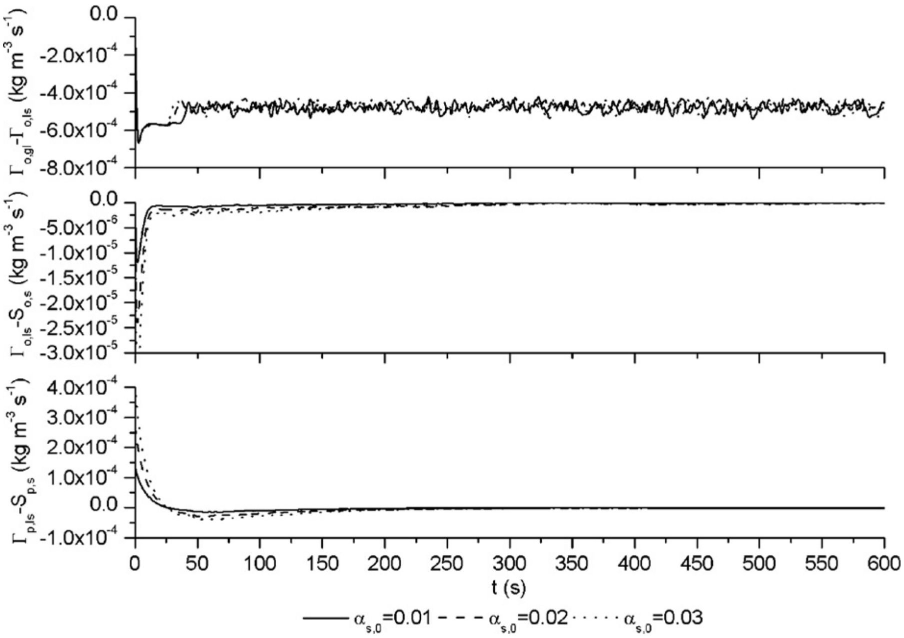

**Fig. 12.** Time courses of volume-averaged $\Gamma_{o,gl}-\Gamma_{o,ls}$, $\Gamma_{o,ls}-S_{o,s}$ and $\Gamma_{p,ls}-S_{p,s}$ under different $\alpha_{s,0}$ = 0.01, 0.02, 0.03 and fixed $U_{g,\mathrm{sup}}$ = 0.02, $C_{p,0}$ = 150 mg/L.

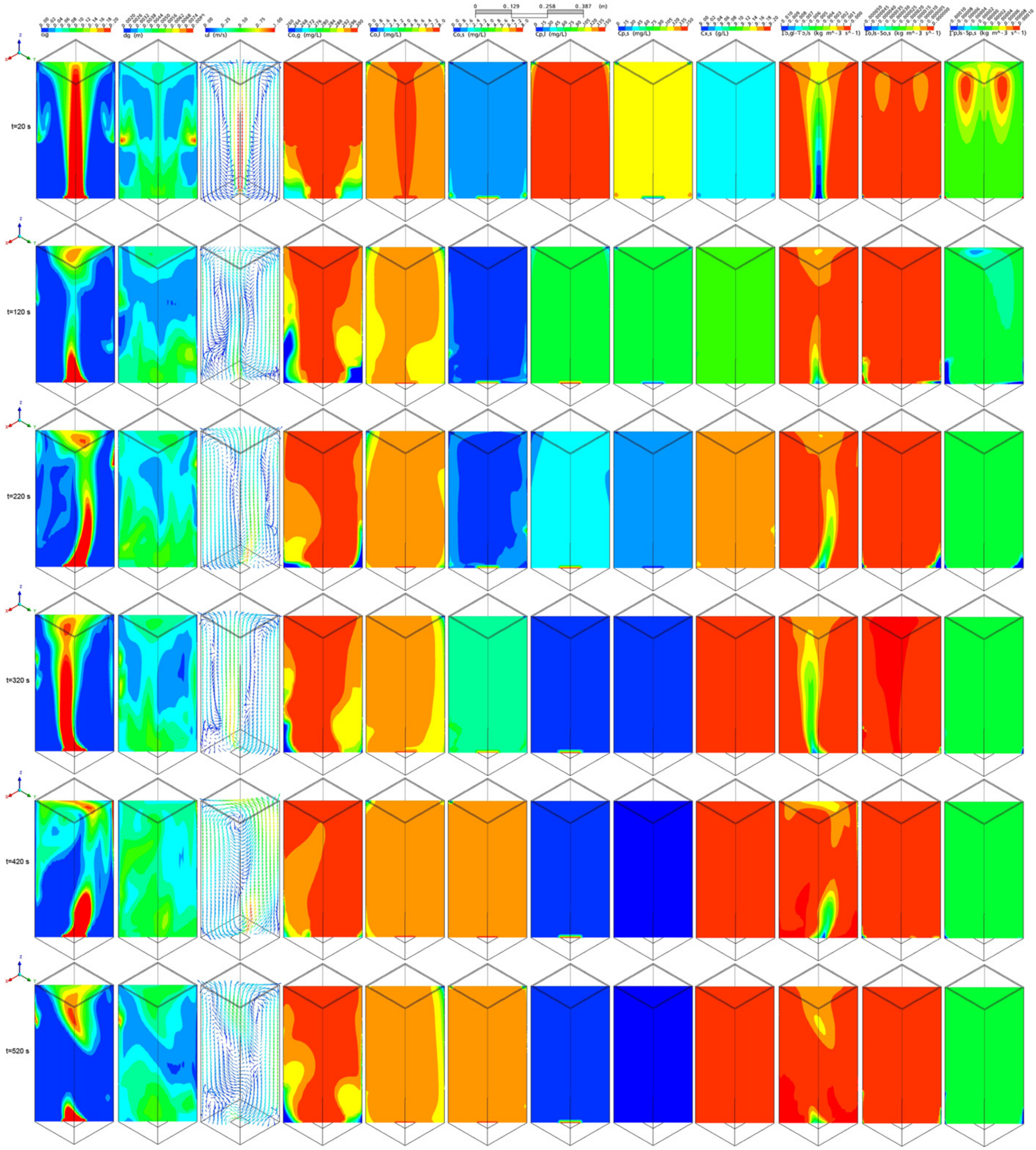

**Fig. 13.** Local transient profiles of dynamic behaviors $\alpha_g$, $d_g$, $\mathbf{u}$, $C_{o,g}$, $C_{o,l}$, $C_{o,s}$, $C_{p,l}$, $C_{p,s}$, $C_{x,s}$, $\Gamma_{o,gl}-\Gamma_{o,ls}$, $\Gamma_{o,ls}-S_{o,s}$, $\Gamma_{p,ls}-S_{p,s}$ under $U_{g,\mathrm{sup}} = 0.02$, $C_{p,0} = 150$ mg/L, $\alpha_{s,0} = 0.02$.

and solid phase cell concentration $C_{x,s}$. Finally, the figures show the volume-averaged species transport comparisons such as the difference between the gas–liquid oxygen mass transfer source and the liquid–solid oxygen mass transfer source $\Gamma_{o,gl}-\Gamma_{o,ls}$, the difference between the liquid–solid oxygen mass transfer source and the solid phase oxygen reaction source $\Gamma_{o,ls}-S_{o,s}$, and the difference between the liquid–solid phenol mass transfer source and the solid phase phenol reaction source $\Gamma_{p,ls}-S_{p,s}$, under different $U_{g,\mathrm{sup}} = 0.01$, 0.02 and 0.03 m/s and constant $C_{p,0} = 50$ mg/L and $\alpha_{s,0} = 0.02$.

The volume-averaged axial liquid flow in the BC is zero as the upward liquid counteracts the downward liquid, but not the velocity itself. Then the volume-averaged $u_w$ can be adopted to evaluate the hydrodynamics of the BC under different operating conditions. However, it is hard to estimate its value considering the interactions between the liquid and the top/bottom of the column, except

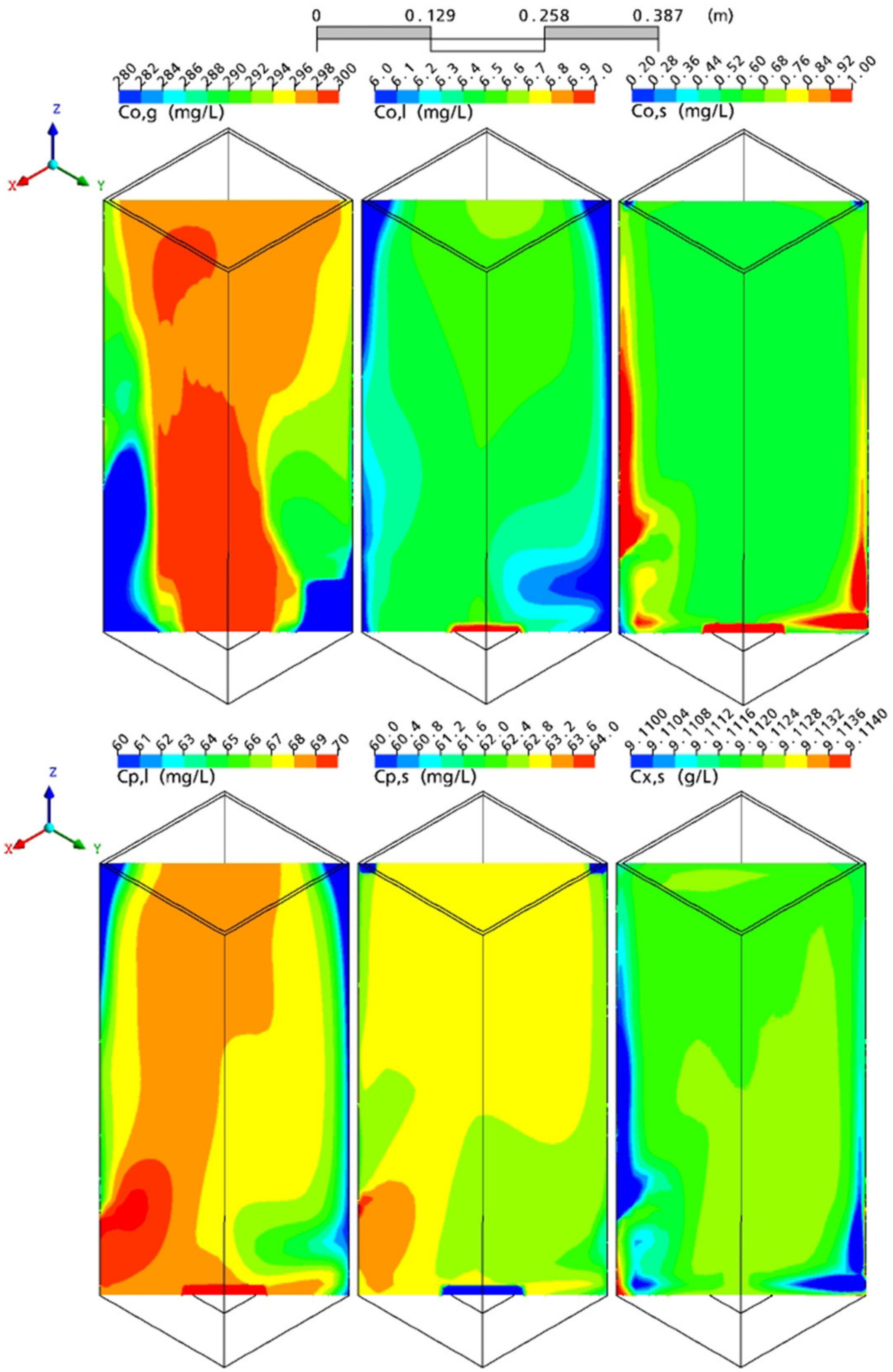

**Fig. 14.** Local transient profiles of species mass concentration profiles $C_{o,g}$, $C_{o,l}$, $C_{o,s}$, $C_{p,l}$, $C_{p,s}$, $C_{x,s}$ under $U_{g,\mathrm{sup}} = 0.02$, $C_{p,0} = 150$ mg/L, $\alpha_{s,0} = 0.02$.

for software calculation. And one should be notified that the BC volume-averaged $u_w$ is the average value of the $u_w$ on the BC weighted by the volume assigned to each point on the BC and thus is a mesh independent result [58].

It is clearly shown that $\alpha_g$ and $u_w$ increase with increasing $U_{g,\mathrm{sup}}$, while $d_g$ remained relatively constant, around 4 mm. In the immobilized batch phenol biodegradation processes, $C_{o,g}$, $C_{o,l}$, $C_{o,s}$ are larger at higher $U_{g,\mathrm{sup}}$, corresponding to higher bioreaction rates, thus smaller $C_{p,l}$ and $C_{p,s}$.

The case is more complex for $C_{x,s}$. During the first half part of the process, the cell growth rate was lower under smaller $U_{g,\mathrm{sup}}$ for smaller $C_{o,s}$ and larger $C_{p,s}$, but higher under smaller $U_{g,\mathrm{sup}}$ during the second half of the process as a result of continuous growth in the presence of residual phenol. The final $C_{x,s}$ was highest for the smallest $U_{g,\text{sup}}$, the reason for which being that more phenol was consumed for cell mass accumulation. As $C_{x,s}$ was much higher than $C_{p,s}$, it can be concluded that most phenol was consumed for cell maintenance rather than for cell growth, according to Eqs. (12) and (13). It should be noted that the changes of $C_{p,l}$ and $C_{p,s}$ were not well controlled under $U_{g,\text{sup}} = 0.03$ m/s, which might be due to the contribution of high turbulence. $\Gamma_{o,gl} - \Gamma_{o,ls}$ and $\Gamma_{o,ls} - S_{o,s}$ were all less than zero throughout, while $\Gamma_{p,ls} - S_{p,s}$ was only larger than zero at the very beginning and less than zero for the rest of the time, which indicates that the interphase mass transfer was the rate-limiting step in most cases.

Figs. 5–8 show the time courses of the volume-averaged $\alpha_g$, $d_g$, $u_W$; $C_{o,g}$, $C_{o,l}$, $C_{p,l}$, $C_{o,s}$, $C_{p,s}$, $C_{x,s}$; $\Gamma_{o,gl} - \Gamma_{o,ls}$, $\Gamma_{o,ls} - S_{o,s}$, $\Gamma_{p,ls} - S_{p,s}$ under different $C_{p,0} = 100, 150, 200$ mg/L and fixed $U_{g,\text{sup}} = 0.02$ m/s, $\alpha_{s,0} = 0.02$. It can be seen that the change in $C_{p,0}$ had little effect on the hydrodynamics and oxygen concentrations in the gas and liquid phases. Larger $C_{p,0}$ needed a longer time for complete biodegradation, corresponding to larger $C_{p,l}$ and $C_{p,s}$ at any time, which resulted in larger $C_{o,s}$ at the beginning of the processes for low consumption rates because of the phenol inhibition effect, and smaller $C_{o,s}$ at the end for higher consumption rates because of the carbon shortage effect. The growth rates of cells under larger $C_{p,0}$ during the first half of the process exhibited little differences but were higher during the second half, resulting in larger $C_{x,s}$ at the end, further indicating that interphase mass transfer was the rate-limiting step and had a more important role than the bioreaction rate. $\Gamma_{o,gl} - \Gamma_{o,ls}$ and $\Gamma_{o,ls} - S_{o,s}$ were relatively unchanged under different $C_{p,0}$, while $\Gamma_{p,ls} - S_{p,s}$ was larger at the beginning of the process, as a result of the higher phenol concentration difference between liquid–solid phases and lower bioreaction rate because of the phenol inhibition effect under larger $C_{p,0}$.

Figs. 9–12 show the time courses of the volume-averaged $\alpha_g$, $d_g$, $u_W$; $C_{o,g}$, $C_{o,l}$, $C_{o,s}$, $C_{p,l}$, $C_{p,s}$, $C_{x,s}$; $\Gamma_{o,gl} - \Gamma_{o,ls}$, $\Gamma_{o,ls} - S_{o,s}$, $\Gamma_{p,ls} - S_{p,s}$ under different $\alpha_{s,0} = 0.01$, 0.02, 0.03 and fixed $U_{g,\text{sup}} = 0.02$ m/s and $C_{p,0} = 150$ mg/L. Changes in the solid loading did not cause significant fluctuations to the volume-averaged hydrodynamic characteristics such as $\alpha_g$, $d_g$ and $u_W$, which may be due to the small amount of the solid particles and its low density. Generally speaking, an increase in $\alpha_{s,0}$ resulted in an increase in the bioreaction, then the decrease in $C_{o,g}$, $C_{o,l}$ and $C_{o,s}$ (except at $\alpha_g = 0.03$), as a combined result of the convection, diffusive and source items in Eq. (4). It was expected that the increase in $\alpha_g$ would cause a significant decrease in the phenol concentrations. However, as the interphase mass transfer was the rate-limiting step and the range of phenol concentrations was much larger than that of oxygen, the change in $C_{p,l}$ and $C_{p,s}$ was mild. Larger $\alpha_g$ meant a larger quantity of cells and smaller $C_{x,s}$ at a given $C_{p,0}$. $\Gamma_{o,gl} - \Gamma_{o,ls}$ was not as sensitive to the change in $\alpha_g$. $\Gamma_{o,ls} - S_{o,s}$ was smaller at larger $\alpha_g$. At the beginning of the processes, $\Gamma_{p,ls} - S_{p,s}$ increased with increasing $\alpha_g$ when it was larger than zero. Subsequently, $\Gamma_{p,ls} - S_{p,s}$ decreased with increasing $\alpha_g$ when it was less than zero.

### 4.2. Model simulation of the local transient process variables

This developed 3D transient CFD model can be applied to simulate the volume-averaged dynamic behaviors of immobilized batch phenol biodegradation processes in a three-phase BC, as described above. The local distribution of the dynamic behaviors within the reactor is of interest because it helps us to better understand the performance of three-phase bioreactions.

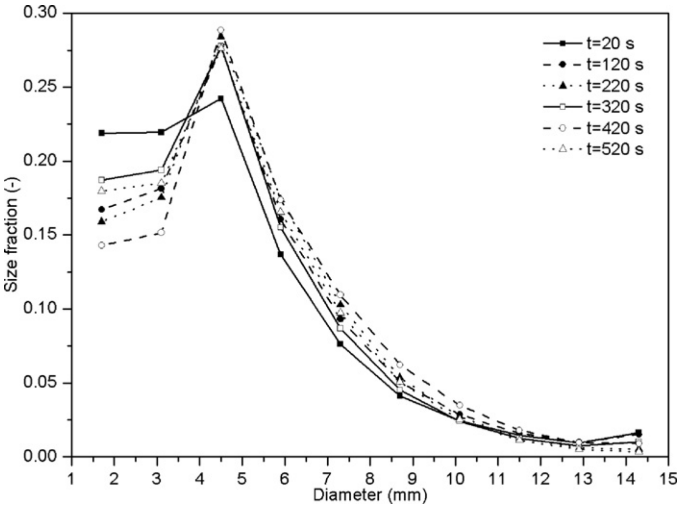

**Fig. 15.** Volume-averaged BSD under $U_{g,\text{sup}} = 0.02$, $C_{p,0} = 150$ mg/L, $\alpha_{s,0} = 0.02$.

Fig. 13 shows the model simulation local transient profiles of the hydrodynamic characteristics such as $\alpha_g$, $d_g$, $\mathbf{u}$, species mass concentrations such as $C_{o,g}$, $C_{o,l}$, $C_{o,s}$, $C_{p,l}$, $C_{p,s}$, $C_{x,s}$ and source differences such as $\Gamma_{o,gl} - \Gamma_{o,ls}$, $\Gamma_{o,ls} - S_{o,s}$, $\Gamma_{p,ls} - S_{p,s}$ under (left to right figures) $U_{g,\text{sup}} = 0.02$ m/s, $C_{p,0} = 150$ mg/L and $\alpha_{s,0} = 0.02$, at (figures in order from top to bottom) $t = 20, 120, 220, 320, 420, 520$ s, respectively. It can be seen from these charts that the gas bubble plume moves back and forth in a pseudo-periodical way, with larger $\alpha_g$ in the central line of the reactor. Near the walls, bubbles are taken downward by the circulation of the liquid as a result of the density difference between the top and the bottom of the reactor. $d_g$ is larger in the regions above the gas distributor and below the surface of the liquid, as a result of bubble breakup and coalescence effects, and also at some locations near the wall as a result of downward bubble accumulation. The distributions of $C_{o,g}$, $C_{o,l}$, $C_{o,s}$, $C_{p,l}$, $C_{p,s}$, $C_{x,s}$ at any locations in the reactor and their concentration changes with time can be illustrated visually by the model prediction. $C_{o,g}$ changes only slightly through the process and has a low value in the corners of the bottom of the column. $C_{o,l}$ experiences a slight decrease and has an almost uniform distribution. $C_{o,s}$ decreases significantly as the phenol biodegradation proceeds and increases at the end when the bioreaction ceases and fluctuations in the distribution of $C_{o,s}$ are not obvious. The cases of phenol degradation and cell growth are as expected and the local distribution is almost uniform in the specified ranges. The local transient profiles of the source differences of $\Gamma_{o,gl} - \Gamma_{o,ls}$, $\Gamma_{o,ls} - S_{o,s}$, $\Gamma_{p,ls} - S_{p,s}$ are also simulated, corresponding to the hydrodynamics and bioreaction characteristics at that instant.

In Fig. 13, species mass concentration ranges are relatively wide to enable better comparisons at different times. However, the local distributions might be ignored at some places where the differences are small. Fig. 14 shows the model prediction of local transient oxygen, phenol and cell concentration profiles at $t = 120$ s. The ranges of $C_{o,g}$, $C_{o,l}$, $C_{o,s}$, $C_{p,l}$, $C_{p,s}$, $C_{x,s}$ are 280–300 mg/L, 6–7 mg/L, 0.2–1.0 mg/L, 60–70 mg/L, 60–64 mg/L and 9.110–9.114 g/L, which are much lower than the ranges of 260–300 mg/L, 0–8 mg/L, 0–8 mg/L, 0–150 mg/L, 0–150 mg/L and 9.0–9.2 g/L in Fig. 13. It can be seen from Fig. 14 that the distribution of $C_{o,g}$ is the most heterogeneous, with higher values in the centre of the bottom and the top and lower values in the corner. It is clear that the distribution of $C_{o,g}$ is very dependent on that of $\alpha_g$. Comparatively, the distribution of $C_{o,l}$ is almost uniform in the main body, except for locations near the wall, which is due to the low $C_{o,g}$ there. The case of the distribution of $C_{o,s}$ is opposite: it has high values near the wall and in the corner, where the bioreaction rates are low. In Fig. 13, there is hardly any visible difference in the distribution of $C_{p,l}$, which exhibits a clear heterogeneous distribution in Fig. 14 within a much smaller range. The distribution of $C_{p,s}$ is not so heterogeneous by comparison, following a similar trend with $C_{p,l}$. The distribution of $C_{x,s}$ is almost

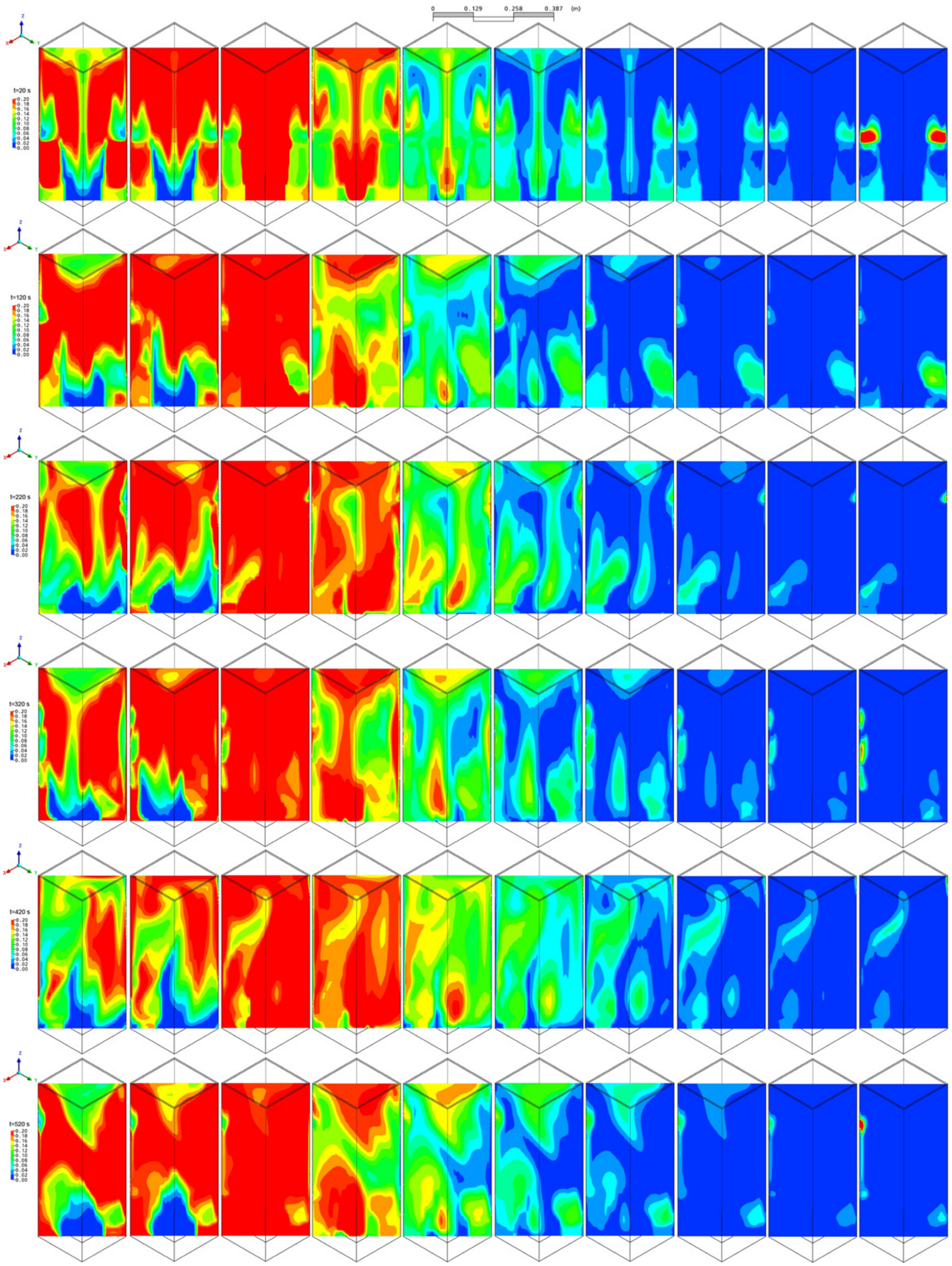

**Fig. 16.** Local transient profiles of BSD under $U_{g,\mathrm{sup}} = 0.02$, $C_{p,0} = 150$ mg/L, $\alpha_{s,0} = 0.02$.

uniform in the main body and has lower values near the wall and in the corner, where some solid beads collect.

From the above two figures, it can be concluded that the developed model can be applied to capture the local transient distributions of the dynamic behaviors of immobilized phenol biodegradation in three-phase BC, including the hydrodynamic characteristics and the species mass concentration profiles, which are very important to understanding and optimizing the performance of the process.

It should be pointed out that, although the distributions of liquid phase oxygen and phenol concentration exhibit heterogeneous phenomena, as shown in Fig. 14, the validation of the volume-averaged model simulated results by experimental measurements in different locations along the column of the reactor is convincing, as the fluctuations of the concentrations are within 7.7% (6.5 ± 0.5 and 65 ± 5 mg/L).

### 4.3. Model simulation of bubble size distributions

Prediction of BSD in the three-phase BC has been achieved previously [1] and in this study, the volume-averaged size fractions of different bubble groups and the local transient profiles of size fraction are also simulated by the developed model for the three-phase bioreaction process, as shown in Figs. 15 and 16, under $U_{g,\text{sup}} = 0.02$ m/s, $C_{p,0} = 150$ mg/L and $\alpha_{s,0} = 0.02$. Fig. 15 shows the volume-averaged BSD at $t = 20$, 120, 220, 320, 420 and 520 s. Small bubbles comprise a large fraction of all bubbles and the 3rd bubble group has the largest value of volume-averaged size fraction, of about 0.28. Fig. 16 shows the model prediction of the local transient profiles of BSD of Groups 1–10 at $t = 20$, 120, 220, 320, 420 and 520 s. It is clear that small bubbles (Groups 1–5) are present throughout the whole reactor and the 3rd group has the largest size fraction of all bubble groups.

## 5. Conclusion

A 3D transient CFD model was developed for simulating the dynamic behaviors of batch phenol biodegradation by immobilized *C. tropicalis* in a three-phase BC, combining three-phase fluid flow, interphase mass transfer and intrinsic bioreaction kinetics, with the MUSIG model adopted to determine the BSD.

Time courses of the volume-averaged hydrodynamic characteristics, species mass concentrations and species transport source term differences were simulated first by the developed model. Model simulation results of oxygen and phenol concentrations in the liquid phase were clearly validated by corresponding experimental measurements. These revealed that interphase mass transfer is the rate-limiting step for the whole biodegradation process in most cases. Local transient profiles of the dynamic behaviors of the three-phase phenol biodegradation processes were predicted reasonably well by the developed CFD model. Detailed analysis of the model simulations revealed that the species mass concentration distributions were controlled both by the dynamic fluctuations of the three-phase hydrodynamics and source term differences. Volume-averaged and local transient BSD were also predicted and these demonstrated that small bubbles comprised a large fraction of bubbles, which is advantageous to the interphase mass transfer and the bioreaction.

Generally speaking, this 3D transient CFD model can be applied to capture the dynamic behaviors of phenol biodegradation in three-phase BCs, which is helpful in optimizing the design and construction of the BC and the operation of the biodegradation process, as well as facilitating scale-up strategies.

## Acknowledgements

The authors wish to acknowledge the financial support provided by the National 973 Project of China (No. 2007CB714302), the International Science and Technology Cooperation Program (No. 2007DFA90530), the National Natural Science Foundation of China (No. 20976124 and No. 20906070), the Natural Science Foundation of Tianjin (No. 07JCZDJC01500), the Research Fund for the Doctoral Program of Higher Education (No. 20060056010), the Key Project of Chinese Ministry of Education, and the Program of Introducing Talents of Discipline to Universities (No. B06006).

## References

[1] X.Q. Jia, J.P. Wen, H.L. Zhou, W. Feng, Q. Yuan, Local hydrodynamics modelling of a gas–liquid–solid three-phase bubble column, AIChE J. 53 (2007) 2221–2231.
[2] K. Bandhyopadhyay, D. Das, P. Bhattacharyya, B.R. Maiti, Reaction engineering studies on biodegradation of phenol by *Pseudomonas putida* MTCC 1194 immobilized on calcium alginate, Biochem. Eng. J. 8 (2001) 179–186.
[3] V.A. Alva, B.M. Peyton, Phenol and catechol biodegradation by the *Haloalkaliphile Halomonas campisalis*: influence of pH and salinity, Environ. Sci. Technol. 37 (2003) 4397–4402.
[4] H. Ozaki, Z. Liu, Y. Terashima, Utilization of microorganisms immobilized with magnetic particles for sewage and wastewater treatment, Water Sci. Technol. 23 (1991) 1125–1136.
[5] L.G. Torres, A. Sánchez-de-la-Vega, N.A. Beltrán, B.E. Jiménez, Production and characterization of a Ca-alginate biocatalyst for removal of phenol and chlorophenols from wastewaters, Process Biochem. 33 (1998) 625–634.
[6] T.S. Chung, K.C. Loh, S.K. Goh, Development of cellulose acetate membranes for bacteria immobilization to remove phenol, J. Appl. Polym. Sci. 68 (1998) 1677–1688.
[7] G. Annadurai, S.R. Babu, K.P.O. Mahesh, T. Murugesan, Adsorption and biodegradation of phenol by chitosan-immobilized *Pseudomonas putida* (NICM 2174), Bioprocess Eng. 22 (2000) 493–501.
[8] T. Brányik, G. Kuncová, J. Páca, The use of silica gel prepared by sol–gel method and polyurethane foam as microbial carriers in the continuous degradation of phenol, Appl. Microbiol. Biotechnol. 54 (2000) 168–172.
[9] T. Godjevargova, Z. Aleksieva, D. Ivanova, Cell immobilization of *Trichosporon cutaneum* strain with phenol degradation ability on new modified polymer carriers, Process Biochem. 35 (2000) 699–704.
[10] U. Beshay, D. Abd-El-Haleem, H. Moawad, S. Zaki, Phenol biodegradation by free and immobilized *Acinetobacter*, Biotechnol. Lett. 24 (2002) 1295–1297.
[11] K.C. Chen, Y.H. Lin, W.H. Chen, Y.C. Liu, Degradation of phenol by PAA-immobilized *Candida tropicalis*, Enzyme Microb. Technol. 31 (2002) 490–497.
[12] T.P. Chung, P.C. Wu, R.S. Juang, Use of microporous hollow fibers for improved biodegradation of high-strength phenol solutions, J. Membr. Sci. 258 (2005) 55–63.
[13] N.K. Pazarlioğlu, A. Telefoncu, Biodegradation of phenol by *Pseudomonas putida* immobilized on activated pumice particles, Process Biochem. 40 (2005) 1807–1814.
[14] K. Bandhyopadhyay, D. Das, B.R. Maiti, Solid matrix characterization of immobilized *Pseudomonas putida* MTCC 1194 used for phenol degradation, Appl. Microbiol. Biotechnol. 51 (1999) 891–895.
[15] A. Mordocco, C. Kuek, R. Jenkins, Continuous degradation of phenol at low concentration using immobilized *Pseudomonas putida*, Enzyme Microb. Technol. 25 (1999) 530–536.
[16] S.L. Pai, Y.L. Hsu, N.M. Chong, C.S. Sheu, C.H. Chen, Continuous degradation of phenol by *Rhodococcus SR* immobilized on granular activated carbon and in calcium alginate, Bioresour. Technol. 51 (1995) 37–42.
[17] J.R. Cleotilde, R.O. Nora, C.U. Elíseo, G.M. Juvencio, Degradation kinetics of phenol by immobilized cells of *Candida tropicalis* in fluidized bed reactor, World J. Microbiol. Biotechnol. 17 (2001) 697–705.
[18] N. Kantarci, F. Borak, K.O. Ulgen, Bubble column reactors, Process Biochem. 40 (2005) 2263–2283.
[19] M. Shishido, T. Kojima, Y.K. Araike, M. Toda, Biological phenol degradation by immobilized activated sludge in gel bead with three-phase fluidized-bed bioreactor, Chem. Eng. Res. Des. Trans. Inst. Chem. Eng. Part A 73 (1995) 719–726.
[20] T.B.M.L. Raja Rao, R.L. Sonolikar, S.P. Saheb, Influence of magnetic field on the performance of bubble columns and airlift bioreactor with submersed microorganisms, Chem. Eng. Sci. 52 (1997) 4155–4160.
[21] A.M. Hannaford, C. Kuek, Aerobic batch degradation of phenol using immobilized *Pseudomonas putida*, J. Ind. Microbiol. Biotechnol. 22 (1999) 121–126.
[22] G. Gonzalez, M.G. Herrera, M.T. Garcia, M.M. Pena, Biodegradation of phenol in a continuous process: comparative study of stirred tank and fluidized-bed bioreactors, Bioresour. Technol. 76 (2001) 245–251.
[23] N. Ruiz-Ordaz, J.C. Ruiz-Lagunez, J.H. Castanon-Gonzalez, E. Hernandez-Manzano, E. Cristiani-Urbina, J. Galindez-Mayer, Phenol biodegradation using a repeated batch culture of *Candida tropicalis* in a multistage bubble column, Rev. Lat. Microbiol. 43 (2001) 19–25.
[24] M. Kotsou, A. Kyriacou, K. Lasaridi, G. Pilidis, Integrated aerobic biological treatment and chemical oxidation with Fenton's reagent for the processing of green table olive wastewater, Process Biochem. 39 (2004) 1653–1660.
[25] J.H. Tay, H.L. Jiang, S.T.L. Tay, High-rate biodegradation of phenol by aerobically grown microbial granules, J. Environ. Eng. 130 (2004) 1415–1423.
[26] J. Galíndez-Mayer, J. Ramón-Gallegos, N. Ruiz-Ordaz, C. Juárez-Ramírez, A. Salmerón-Alcocer, H.M. Poggi-Varaldo, Phenol and 4-chlorophenol biodegradation by yeast *Candida tropicalis* in a fluidized bed reactor, Biochem. Eng. J. 38 (2008) 147–157.
[27] H.A. Jakobsen, H. Lindborg, C.A. Dorao, Modelling of bubble column reactors: progress and limitations, Ind. Eng. Chem. Res. 44 (2005) 5107–5151.
[28] A. Lapin, A. Lübbert, Numerical simulation of the dynamics of two-phase gas–liquid flows in bubble columns reactors, Chem. Eng. Sci. 49 (1994) 3661–3674.
[29] A. Sokolichin, G. Eigenberger, Gas–liquid flow in bubble columns and loop reactors: Part I. Detailed modelling and numerical simulation, Chem. Eng. Sci. 49 (1994) 5735–5746.
[30] E. Delnoij, J.A.M. Kuipers, W.P.M. van Swaaij, Computational fluid dynamics applied to gas–liquid contactors, Chem. Eng. Sci. 52 (1997) 3623–3638.
[31] A. Sokolichin, G. Eigenberger, A. Lapin, A. Lübbert, Dynamic numerical simulation of gas–liquid two-phase flows: Euler/Euler versus Euler/Lagrange, Chem. Eng. Sci. 52 (1997) 611–626.

[32] Y. Pan, M.P. Dudukovic, M. Chang, Numerical investigation of gas-driven flow in 2D bubble columns, AIChE J. 46 (2000) 434–449.

[33] S.M. Monahan, V.S. Vitankar, R.O. Fox, CFD predictions for flow-regime transitions in bubble columns, AIChE J. 51 (2005) 1897–1923.

[34] E. Delnoij, F.A. Lammers, J.A.M. Kuipers, W.P.M. van Swaaij, Dynamic simulation of dispersed gas–liquid two-phase flow using a discrete bubble model, Chem. Eng. Sci. 52 (1997) 1429–1458.

[35] E. Delnoij, J.A.M. Kuipers, W.P.M. van Swaaij, A three-dimensional CFD model for gas–liquid bubble columns, Chem. Eng. Sci. 54 (1999) 2217–2226.

[36] D. Pfleger, S. Gomes, N. Gilbert, H.G. Wagner, Hydrodynamic simulations of laboratory scale bubble columns fundamental studies of the Eulerian–Eulerian modelling approach, Chem. Eng. Sci. 54 (1999) 5091–5099.

[37] S.S. Thakre, J.B. Joshi, CFD simulation of bubble column reactors: importance of drag force formulation, Chem. Eng. Sci. 54 (1999) 5055–5060.

[38] R. Krishna, J.M. van Baten, Eulerian simulations of bubble columns operating at elevated pressures in the churn turbulent flow regime, Chem. Eng. Sci. 56 (2001) 6249–6258.

[39] D. Pfeger, S. Becker, Modelling and simulation of the dynamic flow behavior in a bubble column, Chem. Eng. Sci. 56 (2001) 1737–1747.

[40] V.V. Ranade, Y. Tayalia, Modelling of fluid dynamics and mixing in shallow bubble column reactors: influence of sparger design, Chem. Eng. Sci. 56 (2001) 1667–1675.

[41] P. Spicka, M.M. Dias, J.C.B. Lopes, Gas–liquid flow in a 2D column: comparison between experimental data and CFD modelling, Chem. Eng. Sci. 56 (2001) 6367–6383.

[42] V.S. Vitankar, M.T. Dhotre, J.B. Joshi, A low Reynolds number $k$–$\varepsilon$ model for the prediction of flow pattern and pressure drop in bubble column reactors, Chem. Eng. Sci. 57 (2002) 3235–3250.

[43] N.G. Deen, M. van SintAnnaland, J.A.M. Kuipers, Multi-scale modelling of dispersed gas–liquid two-phase flow, Chem. Eng. Sci. 59 (2004) 1853–1861.

[44] K. Ekambara, M.T. Dhotre, J.B. Joshi, CFD simulations of bubble column reactors: 1D, 2D and 3D approach, Chem. Eng. Sci. 60 (2005) 6733–6746.

[45] W. Feng, J.P. Wen, X.Q. Jia, Q. Yuan, Y. Sun, C.Y. Liu, Modelling for local dynamic behaviors of phenol biodegradation in bubble columns, AIChE J. 52 (2006) 2864–2875.

[46] X.Y. Zhang, G. Ahmadi, Eulerian–Lagrangian simulations of liquid–gas–solid flows in three-phase slurry reactors, Chem. Eng. Sci. 60 (2005) 5089–5104.

[47] G.M. Cartland Glover, S.C. Generalis, Gas–liquid–solid flow modelling in a bubble column, Chem. Eng. Process. 43 (2004) 117–126.

[48] V. Michele, D.C. Hempel, Liquid flow and phase holdup-measurement and CFD modelling for two- and three-phase bubble columns, Chem. Eng. Sci. 57 (2002) 1899–1908.

[49] F. Lehr, D. Mewes, A transport equation for the interfacial area density applied to bubble columns, Chem. Eng. Sci. 56 (2001) 1159–1166.

[50] L. Hagesaether, H.A. Jakobsen, H.F. Svendsen, Modelling of the dispersed-phase size distribution in bubble columns, Ind. Eng. Chem. Res. 41 (2002) 2560–2570.

[51] F. Lehr, M. Millies, D. Mewes, Bubble-size distributions and flow fields in bubble columns, AIChE J. 48 (2002) 2426–2443.

[52] P. Chen, J. Sanyal, M.P. Dudukovic, CFD modelling of bubble columns flows: implementation of population balance, Chem. Eng. Sci. 59 (2004) 5201–5207.

[53] J. Sanyal, D.L. Marchisio, R.O. Fox, K. Dhanasekharan, On the comparison between population balance models for CFD simulation of bubble columns, Ind. Eng. Chem. Res. 44 (2005) 5063–5072.

[54] E.I.V. van den Hengel, N.G. Deen, J.A.M. Kuipers, Application of coalescence and breakup models in a discrete bubble model for bubble columns, Ind. Eng. Chem. Res. 44 (2005) 5233–5245.

[55] E. Olmos, C. Gentric, C. Vial, G. Wild, N. Midoux, Numerical simulation of multiphase flow in bubble column reactors: influence of bubble coalescence and break-up, Chem. Eng. Sci. 56 (2001) 6359–6365.

[56] V.V. VBuwa, V.V. Ranade, Dynamics of gas–liquid flow in a rectangular bubble column: experiments and single/multi-group CFD simulations, Chem. Eng. Sci. 57 (2002) 4715–4736.

[57] I. Banerjee, M. Jayant, K. Modak, K. Bandopadhyay, D. Das, B.R. Maiti, Mathematical model for evaluation of mass transfer limitations in phenol biodegradation by immobilized *Pseudomonas putida*, J. Biotechnol. 87 (2001) 211–223.

[58] ANSYS Canada Ltd., ANSYS CFX-Solver, Release 10.0: Theory, ANSYS Canada Ltd., Waterloo, Canada, 2005.

[59] E.W. Washburn, International Critical Table, McGraw-Hill, New York, 1926.

[60] Y. Jiang, J.P. Wen, H.M. Li, S.L. Yang, Z.D. Hu, The biodegradation of phenol at high initial concentration by the yeast *Candida tropicalis*, Biochem. Eng. J. 24 (2005) 243–247.

[61] A.G. Livingston, H.A. Chase, Modelling phenol degradation in a fluidized-bed bioreactor, AIChE J. 35 (1989) 1980–1992.

[62] M.D. Kumar, S. Jay, J. Anupam, H. Ahmad, A generalized approach to model oxygen transfer in bioreactors using population balances and computational fluid dynamics, Chem. Eng. Sci. 60 (2005) 213–218.

[63] D.C. Arters, L.S. Fan, Solid–liquid mass transfer in a gas–liquid–solid fluidized bed, Chem. Eng. Sci. 41 (1986) 107–115.

[64] N.T. Padial, W.B. VanderHeyden, R.M. Rauenzahn, S.L. Yarbro, Three-dimensional simulation of a three-phase draft-tube bubble column, Chem. Eng. Sci. 55 (2000) 3261–3273.

[65] W. Feng, J.P. Wen, J.H. Fan, Q. Yuan, X.Q. Jia, Y. Sun, Local hydrodynamics of gas–liquid-nanoparticles three-phase fluidization, Chem. Eng. Sci. 60 (2005) 6887–6898.

[66] X.Q. Jia, J.P. Wen, Y. Jiang, X.L. Liu, W. Feng, Modelling of batch phenol biodegradation in internal loop airlift bioreactor with gas recirculation by *Candida tropicalis*, Chem. Eng. Sci. 61 (2006) 3463–3475.

[67] J. Escobedo, G.A. Mansoori, Asphaltene and other heavy-organic particle deposition during transfer and production operations, in: Proceedings-SPE Annual Technical Conference and Exhibition Pi, 1995, pp. 343–358.